

1

The feasibility of using distributed acoustic sensors in surface seismic application

2 **Samir F. Jreij, Whitney J. Trainor-Guitton, and Jim Simmons**

3 Colorado School of Mines,

4 1500 Illinois Ave,

5 Golden, CO, 80401

6 (April 28, 2018)

7 Running head: **The feasibility of using distributed acoustic sensors in surface seismic
application**

ABSTRACT

9 In this paper, an imaging technique that utilizes sparsely sampled, multi-component geophone data
10 and a dense surface distributed acoustic sensor (DAS) acquisition is proposed. The PoroTomo sur-
11 vey at Brady's Natural Lab consisted of 238 multi-component geophones that are spaced anywhere
12 from 60 meters to 150 meters apart. This proves to be a difficult migration problem with such
13 sparse spacing. This paper focuses on identifying a methodology to resolve the spatial sampling
14 issue. Fortunately, the PoroTomo survey consisted of surface DAS cable with an equivalent of 1-
15 meter receiver spacing along the fiber. Both 2-D and 3-D numerical experiments are performed to
16 test the feasibility of using the broadside sensitivity of multi-component geophones and the dense
17 sampling DAS data together to minimize insensitivity to certain waves. In 2-D, a reflectivity model
18 is created from the local fault model in the PoroTomo Survey. This provided a variety of structural
19 dips to test the imaging technique. It was found that using an horizontal force rather than a vertical
20 force with these models produced a much sharper resulting image. A quantitative analysis is further

21 performed to provide an unbiased perspective on the results. The quantitative analysis utilized both
22 energy norm image filtering and a convolutional neural network to prove that distributed sensors add
23 value to imaging efforts with sparsely-sampled, multi-component geophones. The 2-D example is
24 an idealized experiment. A more extreme example is performed in 3-D to confirm the conclusions
25 made in 2-D. A methodology to model DAS data in 3-D is presented prior to showing examples of
26 utilizing the two data types together for imaging. Quantitative analysis is also required for an un-
27 biased perspective on the results. The results from quantitative analysis show that utilizing DAS in
28 surface surveys with a sparse multi-component geophone acquisition proves to be useful in improv-
29 ing the classification accuracy of the image. A more regular experiment must be performed prior to
30 making conclusions about the added value of DAS, so 2-D lines of fiber were utilized instead of the
31 PoroTomo acquisition geometry. The 2-D DAS acquisition increases identifying the true reflectors
32 significantly.

INTRODUCTION

33 Distributed acoustic sensing (DAS) is a technology that uses Rayleigh scattering in a fiber-optic
34 cable to detect elastic signals when wave particle motion is parallel to the sensing fiber (Hornman
35 et al., 2013). The two main components used in distributed sensing are the interrogator unit and the
36 fiber-optic cable. The interrogator unit works as a light source and receiver. It sends a known pulse
37 of light down the fiber. Nearly any type of existing fiber-optic cable can be used in conjunction
38 with an interrogator unit. Small imperfections within the fiber cause backscattering of light. Strain
39 events along the fiber cause this backscattering to change slightly when a wavefield approaches the
40 fiber. The interrogator unit can measure the Rayleigh backscattering and relate it to the strain along
41 the fiber.

42 **DAS Advantages**

43 DAS has many advantages in various industries. For one, DAS is a low-cost acquisition system
44 in wells that already contain fiber optic cables. Even in those wells that do not already contain
45 fiber optic cables, a DAS vertical seismic profile (VSP) is often more affordable than renting and
46 deploying geophones (Mateeva et al., 2014). DAS also enables seismic surveys to be acquired with
47 dense sampling (as small as 10-centimeter receiver spacing) at large distances (tens of kilometers
48 long). Achieving even 1-meter sampling with conventional geophone is expensive and logically
49 difficult. Lastly, DAS has almost perfect repeatability in 4-D surveys when cemented in a borehole
50 or trenched in the subsurface (Mateeva et al., 2013).

51 **DAS Disadvantages**

52 Although DAS may seem like the solution to seismic acquisition, it also has many disadvantages.
53 DAS is most sensitive to waves that have particle motion parallel to the orientation of the fiber, so
54 it is said that the technology has broadside insensitivity. Multi-component geophones also have this
55 issue; with more recording components, however, they are able to resolve more of the wavefield and
56 are not affected by this broadside insensitivity as much.

57 Another disadvantage is that DAS coupling is not trivial in all environments. In a borehole
58 environment, DAS can be cemented behind casing or permanently installed on production tubing
59 (Mateeva et al., 2013). Surface distributed sensor coupling is a more challenging issue. Lindsey
60 et al. (2017) describe how fibers can be utilized in loosely coupled environments. The Stanford
61 Fiber Optic Array consists of a 2.5 km long array that lies in a conduit about 1 to 2 meters below
62 ground. The DAS fiber geometry is restricted by the conduits, though, and the task of installing the
63 fiber is more difficult if there are no existing conduits. Daley et al. (2013) have trenched the cable
64 and returned at a later time to shoot the seismic survey. Although this method is effective, waiting
65 to shoot a survey at a later time can be inconvenient.

66 **Previous Work**

67 Historically, DAS has been used in a borehole environment for flow monitoring, temperature mea-
68 surements, and vertical seismic profiles (Clarke and Sandberg, 1983; Krohn et al., 2000; Mestayer
69 et al., 2011; Barberan et al., 2012; Cox et al., 2012; Daley et al., 2013; Mateeva et al., 2014).

70 Mestayer et al. (2011) describe how permanently installed fiber-optic infrastructure in existing
71 wells can enable low-cost non-intrusive geophysical monitoring. Geophones generally only acquire
72 data along a short subset of the well. This makes repeatable time-lapse surveys difficult as placing

73 the geophones in the same location is not trivial. Mestayer et al. (2011) also discuss how borehole
74 DAS is able to improve repeatability and time-lapse sensitivity because it is able to acquire data
75 along the full well with a single shot. Mateeva et al. (2014) also describe a time lapse, 3-D DAS
76 VSP application. They conclude that DAS has many major business impacts on fields that require
77 enhanced oil recovery (EOR) including cost efficiency, safety, and synergy with other fiber optic
78 applications.

79 Barberan et al. (2012) discuss different ways DAS fiber can be coupled in a borehole environ-
80 ment. DAS fiber can be clamped to production tubing and used as a downhole seismic sensor.
81 Barberan et al. (2012) expand on this explaining that acquiring seismic data over the entire well is
82 essential for acquiring additional transit times for velocity inversion and it allows for a wide range
83 of incidence angles in terms of wave directions that arrive at the fiber for inversion.

84 Daley et al. (2013) describes field tests from both horizontal and borehole distributed sensors.
85 They conclude that the SNR in surface DAS is not sufficient for observing P-waves and that DAS is
86 more useful in borehole environments or longer surface arrays. They don't go into detail, however,
87 regarding why certain waves are not observable in DAS.

88 As seen in these examples, DAS research has emphasized acquiring data in borehole environ-
89 ments because many wells are already equipped with fiber for production. As a result, acquiring
90 DAS in boreholes is as simple as connecting the existing fiber-optic cable to a new interrogator unit
91 that senses acoustic signal. Although there are some studies on surface DAS acquisitions (Daley
92 et al., 2013; Hornman, 2017), there has not been a thorough study in active source experiments.

93 Daley et al. (2013) experiment with a vibroseis injecting a vertical force source. The reflected
94 P-wave is not recorded on the DAS fiber as the experiment only had 1,000 meters of offset, and,
95 therefore, the authors concluded that the SNR in surface DAS is insufficient for observing P-waves

96 due to the relatively small incidental reflected angle. Other source mechanisms must be investigated
97 before such a conclusion can be made about the feasibility of using surface DAS fiber. Another
98 option is utilizing the DAS fiber with geophones to attempt to minimize the insensitivity of some
99 waves. This paper explores different imaging experiments using the field geometry from the Poro-
100 Tomo survey in Northwest Nevada and numerical modeling to explain how DAS fiber can help
101 minimize the insensitivity to waves in conjunction with geophones. The objective of these experi-
102 ments is to analyze if the densely sampled DAS fiber data can help improve the image produced by
103 the sparsely sampled geophones.

104 **PoroTomo Survey**

105 The PoroTomo survey involved four-weeks of data acquisition of geodesy, interferometric syn-
106 thetic aperture radar (InSAR), hydrology, temperature sensing, passive source seismology, and ac-
107 tive source seismology data (Feigl, 2017; Cardiff et al., 2018). The variety of data that were col-
108 lected at the PoroTomo survey lead to the origin of the experiments name: Poroelastic Tomography
109 by Adjoint Inverse Modeling of Data from Seismology, Geodesy, and Hydrology (or PoroTomo for
110 short). These data were jointly collected to characterize and monitor changes in the rock mechanical
111 properties of Brady's Natural Laboratory (BNL), an Enhanced Geothermal System (EGS) reservoir.

112 This paper investigates the active seismic source component of the PoroTomo Experiment. The
113 PoroTomo survey is one of the most unique seismic acquisitions for surface DAS fiber. The survey
114 included 238 multi-component geophones, 156 three-component (vertical and orthogonal horizon-
115 tal) vibroseis source locations that swept from 5 to 80 Hz in 20 seconds, 300 meters of borehole
116 DAS, and nearly nine kilometers of surface fiber-optic cable. The full survey geometry is shown
117 in Figure 1. As seen in Figure 1, the geophones are sparsely spaced with an average spacing of

118 80 meters. This paper focuses on identifying a methodology to resolve the spatial sampling issue.
119 The objective of this paper is to identify if the densely sampled DAS data can help improve the
120 image produced by the sparsely sampled geophones. Both 2-D and 3-D numerical experiments are
121 performed to test the feasibility of using the broadside sensitivity of multi-component geophones
122 and the dense sampling DAS data together to minimize insensitivity to certain waves.

FIBER SENSITIVITY

123 Understanding how DAS fiber works is essential to working with the data that is currently available
124 and to design effective future surveys. For a conventional DAS seismic survey, a known pulse of
125 light is sent into the fiber using an interrogator unit and some of the light is naturally scattered back
126 due to imperfections within the fiber. The interrogator unit is able to record this scattered light along
127 the fiber up to 10-kilometers away. This is known as the base condition inside of the fiber. The fiber
128 undergoes a strain when a seismic wavefield approaches and a scattering of light is produced that is
129 different from the base condition. The interrogator unit is able to relate this new scattering of light
130 to local strain along the fiber by recording the time of arrival and the phase-lag of the returning light
131 signals (Parker et al., 2014).

132 DAS fiber is most sensitive to waves that are able to stretch and squeeze the fiber, so the waves
133 have to have particle motion parallel to the orientation of the fiber. Every seismic sensor has its own
134 distinct sensitivity to the various types of waves depending on their emergent angle. The emergent
135 angle (θ) represents the angle between the incoming wave and the surface of the Earth. Consider a
136 plane wave reflection in the X-Z plane: an emergent angle of 0° represents a wave arriving parallel
137 to the surface (or a plane wave traveling in the Z-direction); an emergent angle of 90° represents a
138 wave arriving perpendicular to the surface (or a plane wave traveling in the X-direction).

139 These points can be demonstrated with a simple 2-D example. Consider wave propagation in
140 the X-Z plane in a homogeneous, flat-layered, isotropic or vertical transverse isotropic medium
141 (Figure 2a-2b). The horizontal DAS fiber is oriented in the x-direction. P-waves have particle
142 motion parallel to the direction of wave propagation (Aki and Richards, 1980). Normal-incidence
143 reflections from a horizontal reflector will arrive perpendicular to the surface fiber. In the case of
144 a 2-D line of horizontal fiber with an vertical vibe, the reflected P-wave will not be seen at short
145 offsets (Figure 2a). The particle motion of P-waves is parallel to the direction of propagation, so
146 at short offsets, the reflected P-wave will arrive perpendicular to the fiber. As seen in Figure 3a,
147 P-waves with a 0° emergent angle show 0 amplitude on fiber and maximum amplitude on the z-
148 component of a geophone, following a $\cos^2(\theta)$ decay with emergent angle (θ). Moving to further
149 offsets yields emergent angles that are at a larger angle to the fiber. According to Figure 3a, these
150 waves will show more data than waves arrive perpendicular to the fiber as they are propagating in
151 the direction of the fiber and less data on the vertical component of the geophone. The further the
152 offset, however, the lower the amplitude of the wave due to attenuation effects.

153 Shear-waves are potentially more interesting when recording with horizontal fiber. Consider
154 again 2-D wave propagation in the X-Z plane in a homogeneous, flat-layered, isotropic or vertical
155 transverse isotropy medium (Figure 2b). SV-waves have particle motion in the X-Z plane, as do
156 P-waves (Aki and Richards, 1980). Normal-incidence reflections from a horizontal reflector will
157 arrive perpendicular to the surface fiber. P-wave particle motion, as stated previously, will be in the
158 z direction, and consequently, will not be recorded by the fiber. SV wave particle motion will be
159 in the x-direction (emergent angle of 0°), and the DAS response will be maximum (Figure 3b). At
160 larger offsets, the SV-wave emerging angle begins to approach 90° . A larger emerging angle means
161 less signal (Figure 3b) is recorded by both the surface DAS and the x-component of the geophone
162 because the SV-wave particle motion approaches perpendicular to these components (Figure 2b).

163 We also consider using SH-waves with the same 2-D survey geometry (homogeneous, flat-
164 layered, isotropic). SH-waves propagate in the X-Z plane. SH waves have particle motion perpen-
165 dicular to the direction of wave propagation or, in this case, in the y-direction. The DAS response
166 to SH-waves will be zero since the SH particle motion is perpendicular to the DAS fiber, in the y-
167 direction. In this 2-D case, the SH-wave will be out of plane regardless of source-receiver offset. In
168 3-D, SH-waves can be seen on the DAS if they are properly oriented. For example, a source-receiver
169 azimuth perpendicular to the 2-D fiber (in this case, in the y-direction) will produce a maximum am-
170 plitude reflection on the DAS since the particle motion is in the x-direction for all offsets. As the
171 source-receiver azimuth moves inline with the fiber, the SH-wave particle motion decreases, and is
172 equal to zero when the source-receiver azimuth is inline with the fiber.

173 In this section, DAS fiber directionality was described analytically and depicted graphically.
174 The directionality is important to understand when creating a seismic survey geometry to assist
175 with geophone deficiencies.

2-D NUMERICAL MODELING EXAMPLES

176 Imaging the geophone data is a difficult task in the PoroTomo Survey due to the irregular spatial
177 sampling and offset. This paper focuses on identifying a way to resolve the spatial sampling issue.
178 Fortunately, the PoroTomo survey includes surface DAS cable that has 10-meter gauge-length and
179 an equivalent of 1-meter receiver spacing along the fiber. Many papers in the literature are interested
180 in methods to convert DAS measurements (strain or strain rate) to a geophone equivalent (particle
181 velocity or displacement) with the intent to replace point sensors with distributed sensors, or use
182 existing geophone processing to clean up DAS data (Daley et al., 2013, 2015; Jreij et al., 2017).
183 The idea of using both data types in simultaneous imaging is explored in this paper to produce more

184 detailed images using synthetic examples.

185 **2-D Synthetic Design**

186 Siler and Faulds (2013) mapped the faults of Brady's Natural Lab shown in Figure 4. It is important
187 to image these faults in detail as they are driving factors behind the recharge of the geothermal
188 reservoir (Feigl, 2017; Folsom et al., 2018). A slice is taken from the Brady's Natural Lab fault
189 model (Siler and Faulds, 2013) in the PoroTomo Survey and used as a reflection velocity models.
190 This slice is shown in Figure 5. The Siler and Faulds (2013) fault model slice is used as a reflectivity
191 model as it contains a variety of structural dips.

192 Seismic sources in the PoroTomo experiment are not on a uniform grid. In fact, the source
193 spacing is as large as 150 meters. Seismic illumination describes how much of the subsurface can
194 be imaged given a source-receiver geometry and velocity model. Illumination in seismic surveys
195 is highly influenced by source-receiver spacing. For the purpose of this section, a constant source
196 spacing of 75 meters (which is about the average source spacing in the PoroTomo survey) is used
197 to minimize migration artifact effects from poor illumination. For the 2-D experiments present in
198 this paper, both vertical and horizontal force sources are modeled to represent a vertically and a
199 horizontally sweeping vibe, respectively, which were also collected at BNL for the PoroTomo field
200 experiment.

201 2-D elastic forward modeling is used to produce strain (as measured by DAS) and displacement
202 (as measured by geophones) data along the surface of our 2-D example excited by a vertical force
203 source. Receivers at every one meter across the experiment are used for recording. As seen in
204 Figure 1, the PoroTomo survey did not include a straight fiber that was this long. It did include,
205 however, a maximum offset of 1,500-meters across the entire survey. For this reason, this whole

206 offset is included for the 2-D example.

207 The code generated for these experiments outputs both strain and displacement at every receiver
208 location. The average geophone spacing is about 70 meters in the PoroTomo experiment. A geo-
209 phone spacing of 100 meters is chosen to analyze geophone spacing closer to the extremes of this
210 experiment. The recorded data are generated from a reflectivity model that is derived from Brady's
211 fault model using an elastic finite difference modeling (FDM) operator from the Madagascar pack-
212 age (Fomel et al., 2013). The next step is to back propagate the recorded data from this forward
213 modeling to recover the receiver wavefield. If this was a field experiment, the field data would be
214 back propagated. Two different sources are needed to create the receiver wavefield. An acceleration
215 force is used for back propagation of the geophone data and a stress tensor is used for back propaga-
216 tion of the DAS data. The proper way to do imaging is to back propagate the two data types (strain
217 and displacement) simultaneously, but this was not possible with current codes, so the data are back
218 propagated individually.

219 The last wavefield that needs to be generated is the source wavefield. The source wavefield is a
220 forward model from the original source location through a smooth velocity model. It is important
221 that the velocity model is smooth as reflections will cause an improper final image. Now, a source
222 and two receiver wavefields exist. An imaging condition is required to combine the wavefields.

223 Traditionally, the zero-lag, cross correlation imaging condition (IC) is used to create a migrated
224 image (Claerbout, 1985). Although this methodology may provide a solution for elastic imaging,
225 this IC produces four resulting images (PP, PS, SP, SS). This proves to be a more difficult compari-
226 son between different data types for the purpose of this paper. Rocha et al. (2016) describes the use
227 of an energy-norm based IC that exploits wavefield directionality to create one final elastic image
228 that represents the measure of reflected energy. There are many other benefits to using the energy-

229 norm IC, but most important for this work is that one final image allows for an easy comparison of
230 migrated elastic data.

231 The image produced from the elastic energy norm RTM with sparsely sampled multi-component
232 geophones using a vertical force is shown in Figure 6a. This image shows reflectors are discontin-
233 uous and difficult to follow. The image is also covered with migration artifacts due to insufficient
234 sampling of the wavefield. An example of this is presented around 800 meters on the x-axis of
235 Figure 6a: the migration artifacts make it difficult for an interpreter to follow the shallow reflector.
236 The deeper reflector in Figure 6a is impossible to identify.

237 The image produced from the elastic energy norm RTM with DAS fiber along the surface of the
238 model creating a virtual receiver at every one meter is shown in Figure 6b. The shallow reflector in
239 this image is sharp and continuous, allowing for easy interpretation. Although migration artifacts
240 are still present around 800 meters on the x-axis, these are different from those experienced in
241 Figure 6a. These migration artifacts are now due to fake modes present because the wavefield is
242 extrapolated using only the x-component data that was recorded with DAS fiber.

243 Now there are two images with two different migration artifacts (i.e. types of noise). The power
244 of stacking the images should theoretically reduce the noise and highlight the reflection events.
245 Linearly stacking the events, however, will not currently work as the amplitudes are on different
246 scales. Instead, the amplitudes of both images are normalized by the maximum and then stacked to
247 produce Figure 6c. Although Figure 6c still has artifacts in it, the reflectors are enhanced and the
248 image is easier to interpret than Figure 6a or Figure 6b.

249 Fiber attributes were discussed earlier in this paper. Different source types can generate dif-
250 ferent polarizations of reflection events. For this reason, the second 2-D experiment uses the same
251 geometry and model as the first experiment, but now an horizontal force is used to generate data.

252 The image produced from elastic energy norm RTM with sparsely sampled multi-component geo-
253 phones and a horizontal force is shown in Figure 7a. This image still shows some discontinuity
254 in reflectors, but the reflector is much easier to follow. The receiver sampling was not changed,
255 so the image is still covered with migration artifacts due to insufficient sampling of the wavefield.
256 On the left-hand side of the geophone image, the end of the dipping fault is not properly imaged.
257 This is due to insufficient aperture in the migration. The deeper reflector is now easier to identify in
258 Figure 7a.

259 The image produced from elastic energy norm RTM with DAS data and an S-source is shown
260 in Figure 7b. The DAS image is still very sharp, but now the migration artifacts have diminished.
261 The deeper reflector is much easier to observe and interpret as well. This image is sharp because the
262 zero-offset SV-wave reflections are perfectly polarized to show the reflectors on DAS and the DAS
263 data is really well sampled.

264 There are two images with two different migration artifacts (i.e. types of noise), so the images
265 are normalized and stacked just as it was done for the previous example. The results are shown in
266 Figure 7c. Figure 7c shows both reflectors clearer than Figure 6c which suggests that a horizontal
267 force is more beneficial for near-offset DAS surveys.

268 **Value of Information**

269 All of the experiments presented in the paper can be qualitatively analyzed and discussed, but quali-
270 tative analysis is always different between people due to different biases and perspectives. A method
271 to quantitatively analyze the experiments is needed to do effective comparisons.

272 The Value of Information (VOI) is a quantitative tool that originates from the field of decision
273 analysis to quantify how relevant and reliable an information source is (Trainor-Guitton et al., 2013).

274 VOI estimates the possible increase in expected utility by gathering information. It is calculated by
 275 comparing the prior value (V_{prior} , the average utility of a decision made with current information)
 276 to the value with imperfect information ($V_{imperfect}$) by subtracting the two, shown in Equation 1.

$$VOI = V_{imperfect} - V_{prior} \quad (1)$$

277 The goal of this project is to observe if there is any added value to using distributed acoustic
 278 sensing in surface acquisitions. The value with imperfect information shown in Equation 2 can only
 279 be calculated with a quantitative measure of how accurate the information source is.

$$V_{imperfect} = \sum_{j=F,NF} Pr(\theta^{int} = \theta_j) \max_a [\sum_{i=F,NF} Pr(\theta = \theta_i | \theta^{int} = \theta_j) v_a(\theta_i)] \quad (2)$$

280 This quantitative measure can be represented by the posterior probability, $Pr(\theta = \theta_i | \theta^{int} = \theta_j)$,
 281 within the value with imperfect information (Equation 2). Specifically for these problems, the
 282 posterior probability can be how often interpretations of faults align with the actual presence of
 283 faults. It is important to calculate the posterior reliability so the value of imperfect information can
 284 be completed. The posterior probability can be calculated using Equation 3,

$$Pr(\theta = \theta_i | \theta^{int} = \theta_j) = \frac{(Pr(\theta = \theta_i)) Pr(\theta^{int} = \theta_j | \theta = \theta_i)}{Pr(\theta^{int} = \theta_i)}; \forall i, j = F, NF \quad (3)$$

285 where θ represents a true value of Fault or Not Fault, θ^{int} represents an interpreted Fault or Not
 286 Fault. There are a variety of methodologies to produce information about whether an interpreted
 287 fault is actually a fault or not. This paper utilizes a machine learning approach to interpret the
 288 features in the migrated image.

289 **Convolutional Neural Network Analysis**

290 Machine learning is a field within computer science that focuses on the ability of computer systems
291 to learn patterns within data without being explicitly programmed for these patterns (Samuel, 1959).
292 Machine learning has had a large boom in the geophysics industry within the last 10 years.

293 There are a variety of machine learning algorithms that can be utilized based on the problem that
294 needs to be solved. One of the most powerful machine learning algorithms is the neural network.
295 Neural networks are inspired by the biological neural networks that constitute human brains or at
296 least how humans perceive they work (Gerven and Bohte, 2018). They consist of many layers in
297 parallel and every layer consists of a number of nodes. All neural networks consist of at least two
298 layers: the input layer and output layer. All the extra layers in between the input and output layers
299 are the hidden layers. The nodes of every layer are like neurons in the brain. Every neuron has its
300 own activation function that determines whether it should be “fired” or not similar to how a neuron
301 in the brain behaves. Each layer receives the output from the previous layer based on if the previous
302 neuron is fired or not.

303 Convolutional Neural Networks (CNN) in particular are at the core of most state-of-the-art com-
304 puter vision solutions for a wide variety of tasks. One of the most accurate CNN image classifiers
305 is the Inception-v3 model (Szegedy et al., 2015). The original Inception-v3 model is trained and
306 tested on the 2012 ImageNet Large Scale Visual Recognition Challenge (Russakovsky et al., 2015).
307 The training dataset consisted of 10,000,000 labeled images that depicted 1,000 object categories.
308 The Inception-v3 model was able to perform with 3.5% top-5 error, meaning that the target label
309 is within the top-5 probability classifications that the algorithm produced. A top-5 error of 3.5%
310 means the Inception-v3 model is able to perform with high accuracy, making it a top contender for
311 a geophysics image classification problem.

312 The Inception-v3 model utilizes transfer learning which means it stores knowledge gained from
313 training on the ImageNet dataset and then applies it to a different but related problem. It is difficult
314 to train a CNN from scratch because a large dataset is needed with a substantial amount of machines
315 equipped with GPU's. Instead, the intermediate layers of the Inception-v3 model are used as they
316 are already trained on detecting edges, shapes, and other high level features. The weights of the
317 model's last layer are recreated to identify if an image is either a fault or not a fault.

318 The Inception v3 model's ability to identify features can be leveraged within the geophysics
319 realm. The first step is to create some training data to retrain the model. The objective is to see
320 if DAS helped identify more faults than a sparse array of multi-component geophones. For the
321 experiments in this chapter, RTM images are created from 2-D reflectivity slices of the Siler and
322 Faulds (2013) fault model. There are about 500 other slices along both the X and Y axis of the
323 PoroTomo grid. A number of these slices can be migrated to create training data for identifying
324 faults.

325 The next step is to take windows of the migrated images and label them based on if there are
326 faults or not within the image. 100 meter by 100 meter (10 grid cell by 10 grid cell) subsets of the
327 migrated images were created. There are a large amount of data present and individually picking
328 whether an image contains a fault or not would take a long time. As stated earlier, the true fault
329 model exists to compare with the migrated images. The same subset of the migrated images can
330 be compared with the reflectivity model. If more than half the pixels are a fault, then the program
331 labels the training data as a fault (Figure 8a). Otherwise, the program labels the training data as not
332 a fault (Figure 8b).

333 This is an easy and automatic way to generate training data, but training is an essential step
334 prior to testing, so it needs to be continually improved. The next step is to QC the training data to

335 make sure that the examples are actually of “faults” and “not faults”. There is a lot of back and forth
336 until an acceptable cross-validation accuracy is achieved. A total of 2500, 100 meter by 100 meter
337 windowed RTM images were used to train the CNN to detect faults. A final training validation
338 accuracy of 94.4% is achieved. This is an acceptable accuracy check and now the neural network is
339 ready to be tested on data that were not included in the training data.

340 A 100 meter by 100 meter testing data is created the same way the training data is created. The
341 testing data is kept hidden from the training data. The first RTM image that is used for testing is
342 the vertical source data from the velocity model shown in Figure 5. The first test is on the sparse,
343 multi-component geophone image (Figure 6a). The RTM image is decomposed into 3,625 (100
344 meter x 100 meter) images with labels of “Faults” and “Not Faults”. This same process is used for
345 the synthetic created from DAS and multi-component geophones.

346 A posterior reliability of information can be calculated with the results from the testing data.
347 The resulting posterior reliability of information is shown graphically in Figure 9a and Figure 9b
348 for a vertical force and a horizontal force, respectively.

349 The results from Figure 9a for the vertical source show that adding DAS into the sparse array of
350 geophones with 5 as the velocity model improves the classification of faults by 20%. However, there
351 is an increase in false negatives by about 30%. This means either the normalized, stacked image
352 has many artifacts or the classifier needs to be better trained on what is not a fault. The number of
353 false positives decreases by 20% which is a substantial amount. Lastly, the number of true negatives
354 decreases by almost 30%. This confirms that the classifier needs to be better trained on what is not
355 a fault.

356 The results from Figure 9b for the horizontal source show that adding DAS into the sparse
357 array of geophones with 5 as the velocity model decreases the classification of faults by about 1%.

358 However, the classification of true negatives increases by about 5% and false negatives decreases by
359 about 5% meaning the DAS data did add some value to the CNN classification.

360 **2-D Summary**

361 This section discussed in great detail how 2-D DAS data can be modeled. It also showed how a long
362 offset, 2-D surface DAS line can produce a sharp resulting image. A quantitative analysis using
363 a machine learning methodology showed that DAS does add value to sparse geophone arrays. A
364 quantitative analysis also shows that using a horizontal force with DAS allows for sharper images.
365 These hypotheses must now be confirmed with a 3-D acquisition.

3-D NUMERICAL MODELING EXAMPLES

366 The objective of this paper is to observe if there is any added value of using surface DAS with
367 sparsely sampled, multi-component geophones. In the previous section, we observed that in a long
368 2-D line, there is added value using DAS to help with the spatial sampling. In 3-D, however, there
369 are many more complications than in 2-D. This section explores additional examples of using DAS
370 in combination with multi-component geophones, but now with the PoroTomo 3-D survey geometry.
371 These examples utilize numerical modeling to understand more about what is recorded.

372 A velocity model from sweep interferometry shown in Figure 10 was used to create data (Matzel
373 et al., 2017a). As in the previous section, a modified version of the conventional elastic FDM code
374 (ewefdm) present in Madagascar (Fomel et al., 2013) is utilized, but now for the 3-D case. This
375 allows us to recover both displacement and strain data along receivers in the grid. A variable density
376 is now used to create reflectivity instead of using purely velocity changes to create reflectivity in the
377 2-D case.

378 **3-D Modeling of Non-Uniform DAS Acquisition**

379 The wavefield along the fiber is now recorded for the six components of strain (XX, XY, XZ, YY,
 380 YZ, and ZZ). Field DAS data with single fiber, however, does not recover all six components. In-
 381 stead, it only recovers contributions of the wavefield in the direction that it is oriented. We can
 382 project the six components from the synthetic data on to the vector direction of the field fiber loca-
 383 tions to recover the strain in the direction that the fiber is oriented by using Equation 4,

$$\begin{bmatrix} \varepsilon_{ZZ} \\ \varepsilon_{XX} \\ \varepsilon_{YY} \\ \varepsilon_{XY} \\ \varepsilon_{YZ} \\ \varepsilon_{ZX} \end{bmatrix} = \begin{bmatrix} V_Z^2 & V_X^2 & V_Y^2 & 2V_XV_Y & 2V_YV_Z & 2V_ZV_X \end{bmatrix} = \begin{bmatrix} \varepsilon' \end{bmatrix} \quad (4)$$

384 where ε_{ij} is the strain in the direction ij , V_i is the vector projection in the i direction, and ε' is
 385 the strain in the direction of the fiber.

386 A matrix of fiber vector directions must be created prior to using Equation 4. The fiber endpoints
 387 were recorded in the field using a handheld GPS device after the fiber was trenched. The virtual
 388 receiver locations along the fiber were then interpolated at 1-meter spacing between these endpoints.
 389 Although this gives a good estimate of the x and y coordinates of the fiber, this does not give any
 390 information on how deep the fiber was trenched. For this reason, we assume that the fiber was
 391 all trenched in the same horizontal plane and there are no dips along the fiber. This simplifies
 392 Equation 4 to only have contributions from X and Y.

393 Applying Equation 4 recovers only one value of strain along the fiber. In reality, there are

394 contributions from both X and Y, so the strain matrix should have values at XX, YY, and XY. We
 395 can use the adjoint operation to recover a vector projection of the strain value from Equation 4. The
 396 adjoint operation shown in Equation 5 returns back to the original PoroTomo coordinate system.

$$\begin{bmatrix} \varepsilon' \end{bmatrix} = \begin{bmatrix} V_Z^2 \\ V_X^2 \\ V_Y^2 \\ 2V_X V_Y \\ 2V_Y V_Z \\ 2V_Z V_X \end{bmatrix} = \begin{bmatrix} \varepsilon_{ZZ} \\ \varepsilon_{XX} \\ \varepsilon_{YY} \\ \varepsilon_{XY} \\ \varepsilon_{YZ} \\ \varepsilon_{ZX} \end{bmatrix} \quad (5)$$

397 The last attribute of fiber that needs to be modeled is the gauge-length. As discussed earlier
 398 in this paper, the gauge-length of fiber is related to the wavelength recorded along the fiber and it
 399 acts as a moving average. The gauge-length in the PoroTomo survey was set at 10-meters, so the
 400 modeled data, d , is a matrix multiplication of $\frac{1}{10}$ for the gauge length, the spatial sampling 1-meter,
 401 and the raw point data, b , recorded by the finite difference code (shown in Equation 6, after Lim
 402 Chen Ning and Sava, 2018).

$$\begin{bmatrix} d_5 \\ d_6 \\ d_7 \\ \vdots \\ d_{n-5} \end{bmatrix} = \frac{1}{10} \begin{bmatrix} 1 & 1 & 1 & 1 & 1 & 1 & 1 & 1 & 1 & 1 & 0 & 0 & 0 & 0 \\ 0 & 1 & 1 & 1 & 1 & 1 & 1 & 1 & 1 & 1 & 1 & 0 & 0 & 0 \\ 0 & 0 & 1 & 1 & 1 & 1 & 1 & 1 & 1 & 1 & 1 & 0 & 0 & 0 \\ 0 & 0 & 0 & \ddots & 0 \\ 0 & 0 & 0 & 0 & 1 & 1 & 1 & 1 & 1 & 1 & 1 & 1 & 1 & 1 \end{bmatrix} \begin{bmatrix} b_5 \\ b_6 \\ b_7 \\ \vdots \\ b_{n-5} \end{bmatrix} \quad (6)$$

403 **Numerical Modeling**

404 It is important to image the faults in detail at Brady's Natural Lab as they are the driving factors
405 behind the recharge of the geothermal reservoir. Although Siler and Faulds (2013) would be a good
406 candidate for data modeling, a simpler model is needed to first test the hypothesis of imaging using
407 the two data types simultaneously. A four layer model with a variety of structures is used as the
408 density model for the first example (Figure 11). There is a contrast of about 300 g/cc between each
409 layer to ensure strong reflections.

410 The synthetic images are produced using the same methodology presented in the 2-D section.
411 The results from migrating the DAS data are shown in Figure 12. The results from migrating the
412 geophone data are shown in Figure 13. A visual reflectivity model shown on the left of both figures
413 was produced by applying the Laplacian operator on Figure 11 and setting all values to one.

414 At first glance, it seems as if the DAS image does not have any reflectors. It can be compared
415 to the true reflectivity model shown on the right of Figure 12 to identify the signal in the image. It
416 is clear that the data recorded by the DAS fiber is too low in frequency to resolve the beds within
417 the image. This is due to both the velocity field that the experiment used to mimic the PoroTomo
418 subsurface and the FDM accuracy condition presented in Equation 7.

$$\frac{v_{min}}{f_{max}} > N * \sqrt{dx^2 + dy^2 + dz^2} \quad (7)$$

419 The minimum velocity of approximately 950 m/s from the input velocity field forces the maxi-
420 mum frequency of the wavelet to be 16 Hz and the peak frequency of the wavelet to be 12 Hz. This
421 equates to a 12 Hz wavelet and the velocity model corresponds to a wavelength of about 108 meters.

422 The DAS image (Figure 12) is also contaminated by fake modes and migration artifacts (Rocha

423 et al., 2016). Fake modes are expected since the displacement field is incomplete when wavefield
424 extrapolation was performed as the fiber is only recording one component of strain in the direction
425 that it is oriented. An inexperienced interpreter would eagerly interpret the fake modes as an area
426 of interest for further exploration methods.

427 At first glance, the geophone data also appear to have no clear reflection events. The image can
428 again be compared to the true reflectivity model overlain on the left of Figure 13 to identify the
429 signal in the image. The geophone image is also limited by the source wavelet that was injected
430 into the model. Differentiation between the thin beds is not possible using the source wavelet in this
431 experiment.

432 The geophone image, similar to the DAS image, is also contaminated by migration artifacts.
433 These migration artifacts, however, are due to the insufficient sampling that creates migration ar-
434 tifacts on the edge of reflectors. The wavefield is not sampled completely because the geophones
435 adopted from the PoroTomo survey are placed sparsely around the model (the average geophone
436 spacing is about 80 meters).

437 **Quantitative Image Comparison**

438 In 2-D, a machine learning methodology was used to create a quantitative image comparison. Al-
439 though 3-D CNN's exist, they are not as polished and available as 2-D CNN's. Instead, the data
440 are quantitatively analyzed using energy norm image filtering. Energy norm filtering focuses on
441 highlighting areas with reflected energy is maximum, so filtering the image based on an applied
442 limit will highlight where reflections may be coming from as opposed to migration artifacts. The
443 geophone and DAS images are combined by first normalizing the data types based on their maxi-
444 mum amplitude. They are then stacked together to test this hypothesis. This image would ideally

Table 1: Confusion matrix for top 90% energy reflected.

Top 90% energy reflected		
	θ_R^{int}	θ_{NR}^{int}
θ_R	184800	1206000
θ_{NR}	346700	1824000

445 highlight continuous reflectors with the densely sampled DAS data and reduce migration artifacts
 446 by extrapolating the full displacement wavefield with the multi-component geophones.

447 Every model cell that is above an applied limit is assigned a value of 1 and every model box that
 448 is below the limit is assigned a value of 0. A cell-by-cell comparison between the filtered, multi-
 449 component geophone image and the original reflectivity model is performed to identify how much
 450 additional accuracy is gained by adding the DAS data. The results of this cell-by-cell comparison
 451 are presented in confusion matrix form (Table 1), where R represents reflections and NR represents
 452 not reflections.

453 The confusion matrices assist in calculating the posterior value using Equation 3. The posterior
 454 value explains the probability that an event which the data type predicted is the event present. The
 455 posterior can then be used to calculate the utility or value of information added when using DAS
 456 and geophone versus only geophone with Equation 1. The results for the medium filter, posterior
 457 values in the four layer model presented in this paper are displayed in Figure 14.

458 In this experiment, adding distributed sensors increases the probability of finding if a cell is not
 459 a reflector and decreases the probability of false negatives. Adding distributed sensors, however,
 460 increases the probability of identifying false positives and decreases the probability of finding true
 461 reflectors. This experiment, however, is inconclusive in identifying if DAS has added value with
 462 sparsely sampled geophone data. A better DAS geometry must be tested to make further conclusions

463 on the effectiveness of surface DAS fiber.

464 The geometry shown in Figure 15 is utilized to further test the effectiveness of surface DAS
465 fiber. This new acquisition utilizes 25% less fiber and 60% less sources than the PoroTomo survey
466 geometry. Quantitative analysis using the energy norm filtering methodology is utilized again to
467 identify how well the survey imaged. The results are presented in Figure 16

468 Figure 16 shows a significant increase in true positives and decrease in false negatives. Al-
469 though there was an increase in false positives and a decrease in true negatives, the increase in true
470 positives proves that this new acquisition is better suited to image the subsurface with surface DAS
471 fibers. Energy norm imaging again allowed for an automatic method to interpret images output
472 from the migration images. Filtering images based on amplitudes is a crude approximation of how
473 an interpreter would “interpret” an image.

474 **Summary**

475 This section discussed differences in modeling DAS data in 3-D versus 2-D. The experiments in
476 this section helped clarify what kinds of data that a single surface DAS fiber can record. The ex-
477 periments discovered that the DAS configuration in the PoroTomo survey combined with the low
478 frequency nature of the modeling did not add value to the multi-component geophone imaging ef-
479 fort. Additionally, the percentages of missing strain components in 3-D is larger than the 2-D case,
480 contributing to the poor image quality. A better geometry and multi-component DAS were required
481 to make further conclusions on the effectiveness of DAS fiber in surface acquisition. Another ex-
482 periment was preformed with DAS fibers arranged in 2-D lines. This acquisition geometry led to
483 an increased percentage of reflectors identified. It is concluded that the 2-D surface DAS fiber lines
484 are a better suited geometry to image the subsurface.

CONCLUSIONS

485 In this paper, we discussed some of the fiber attributes that are essential to understand before looking
486 at surface DAS data. The most important attribute is the types of waves that fiber is directionally
487 sensitive. It is concluded that surface DAS in a flat-layered Earth model is sensitive to long offset
488 P-waves, short offset SV-waves, and SH-waves produced by a source that is perpendicular to the
489 fiber orientation.

490 It was discovered that the geophone data in the PoroTomo survey was too sparsely sampled, and
491 the hypothesis that densely sampled DAS data can fill in the gaps of the geophones was introduced.
492 This hypothesis was tested in 2-D using elastic numerical modeling and RTM. It is then shown how
493 data are modeled for DAS receivers in 2-D. The energy norm imaging condition was chosen as it
494 allowed for an easier method to compare two images than the conventional imaging condition. The
495 experiments showed that an inline horizontal force allows for the best results qualitatively. Lastly,
496 this section explains the need for statistical and quantitative analysis in the geophysics realm. A de-
497 scription of how to perform quantitative analysis using machine learning methodology is presented.
498 Both methods concluded that DAS added imaging value to sparsely sampled multi-component geo-
499 phones.

500 The 2-D scenario did not test the full DAS fiber directionality. We discuss 3-D numerical mod-
501 eling and RTM used to combine DAS and multi-component geophone data. The challenges of
502 modeling DAS in 3-D are also discussed including recording the proper component of strain along
503 the fiber. The resulting migrated images did not clarify if DAS added any qualitative value to multi-
504 component geophone images as the migrated images were too low of a frequency to analyze due to
505 the limitation of the velocity model. A quantitative analysis of the combined image is utilized. This
506 chapter concluded that adding DAS data only helped to reduce the number of false positives by a

507 very small fraction. This experiment is inconclusive in regards to identifying if DAS can add value
508 to sparsely sampled geophone data, so another experiment was performed with 2-D surface DAS
509 fiber lines. The new proposed experiment with long-offset, 2-D surface fiber lines concluded that
510 using the new geometry was better suited for surface DAS acquisitions. The next proposed step is
511 to test this hypothesis with field data.

REFERENCES

- 512 Aki, K., and P. G. Richards, 1980, Quantative seismology: Theory and methods: New York, **801**.
- 513 Barberan, C., C. Allanic, D. Avila, J. Hy-Billiot, A. Hartog, B. Frignet, and G. Lees, 2012, Multi-
- 514 offset seismic acquisition using optical fiber behind tubing: Presented at the 74th EAGE Confer-
- 515 ence and Exhibition incorporating EUROPEC 2012.
- 516 Cardiff, M., D. D. Lim, J. R. Patterson, J. Akerley, P. Spielman, J. Lopeman, P. Walsh, A. Singh, W.
- 517 Foxall, H. F. Wang, et al., 2018, Geothermal production and reduced seismicity: Correlation and
- 518 proposed mechanism: Earth and Planetary Science Letters, **482**, 470–477.
- 519 Claerbout, J. F., 1985, Imaging the earth's interior: Blackwell scientific publications Oxford, **1**.
- 520 Clarke, R., and C. L. Sandberg, 1983, Fiber optic temperature sensing. (US Patent 4,417,782).
- 521 Cox, B., P. Wills, D. Kiyashchenko, J. Mestayer, J. Lopez, S. Bourne, R. Lupton, G. Solano, N.
- 522 Henderson, D. Hill, et al., 2012, Distributed acoustic sensing for geophysical measurement, mon-
- 523 itoring and verification: **37**, 7–13.
- 524 Daley, T., D. Miller, K. Dodds, P. Cook, and B. Freifeld, 2015, Field testing of modular borehole
- 525 monitoring with simultaneous distributed acoustic sensing and geophone vertical seismic profiles
- 526 at citronelle, alabama: Geophysical Prospecting.
- 527 Daley, T. M., B. M. Freifeld, J. Ajo-Franklin, S. Dou, R. Pevzner, V. Shulakova, S. Kashikar, D. E.
- 528 Miller, J. Goetz, J. Henninges, et al., 2013, Field testing of fiber-optic distributed acoustic sensing
- 529 (das) for subsurface seismic monitoring: The Leading Edge, **32**, 699–706.
- 530 Feigl, K. L., 2017, Overview and preliminary results from the porotomo project at brady hot springs,
- 531 nevada: Poroelastic tomography by adjoint inverse modeling of data from seismology, geodesy,
- 532 and hydrology: Presented at the Stanford Geothermal Workshop.
- 533 Folsom, M., J. Lopeman, D. Perkin, and M. Sophy, 2018, Imaging shallow outflow alteration to
- 534 locate productive faults in ormats bradys and desert peak fields using csamt.

- 535 Fomel, S., P. Sava, I. Vlad, Y. Liu, and V. Bashkardin, 2013, Madagascar: Open-source software
536 project for multidimensional data analysis and reproducible computational experiments: Journal
537 of Open Research Software, **1**.
- 538 Gerven, M. V., and S. Bohte, 2018, Artificial Neural Networks as Models of Neural Information
539 Processing.
- 540 Hornman, J., 2017, Field trial of seismic recording using distributed acoustic sensing with broadside
541 sensitive fibre-optic cables: Geophysical Prospecting, **65**, 35–46.
- 542 Hornman, K., B. Kuvshinov, P. Zwartjes, and A. Franzen, 2013, Field trial of a broadside-sensitive
543 distributed acoustic sensing cable for surface seismic: Presented at the 75th EAGE Conference
544 & Exhibition incorporating SPE EUROPEC 2013.
- 545 Jreij, S., W. Trainor-Guitton, D. Miller, et al., 2017, Field data comparison of 3d horizontal dis-
546 tributed acoustic sensing and geophones: SEG Technical Program Expanded Abstracts.
- 547 Krohn, D. A., T. MacDougall, and A. Mendez, 2000, Fiber optic sensors: fundamentals and appli-
548 cations: Isa.
- 549 Lindsey, N. J., E. R. Martin, D. S. Dreger, B. Freifeld, S. Cole, S. R. James, B. L. Biondi, and J. B.
550 Ajo-Franklin, 2017, Fiber-optic network observations of earthquake wavefields: Geophysical
551 Research Letters.
- 552 Mateeva, A., J. Lopez, J. Mestayer, P. Wills, B. Cox, D. Kiyashchenko, Z. Yang, W. Berlang, R.
553 Detomo, and S. Grandi, 2013, Distributed acoustic sensing for reservoir monitoring with vsp:
554 The Leading Edge, **32**, 1278–1283.
- 555 Mateeva, A., J. Lopez, H. Potters, J. Mestayer, B. Cox, D. Kiyashchenko, P. Wills, S. Grandi, K.
556 Hornman, B. Kuvshinov, et al., 2014, Distributed acoustic sensing for reservoir monitoring with
557 vertical seismic profiling: Geophysical Prospecting, **62**, 679–692.
- 558 Matzel, E., X. Zeng, C. Thurber, Y. Luo, C. Morency, et al., 2017a, Seismic interferometry using

559 the dense array at the brady geothermal field.

560 Matzel, E. M., X. Zeng, C. Thurber, and C. Morency, 2017b, Using Virtual Earthquakes to Charac-

561 terize the Material Properties of the Brady Hot Springs , Nevada: Geothermal Resources Council.

562 Mestayer, J., B. Cox, P. Wills, D. Kiyashchenko, J. Lopez, M. Costello, S. Bourne, G. Ugueto,

563 R. Lupton, G. Solano, et al., 2011, Field trials of distributed acoustic sensing for geophysical

564 monitoring, *in* SEG Technical Program Expanded Abstracts 2011: Society of Exploration Geo-

565 physicists, 4253–4257.

566 Parker, T., S. Shatalin, and M. Farhadiroushan, 2014, Distributed Acoustic Sensing - A new tool for

567 seismic applications: First Break, **32**, 61–69.

568 Rocha, D., N. Tanushev, and P. Sava, 2016, Isotropic elastic wavefield imaging using the energy

569 norm: Geophysics, **81**, S207–S219.

570 Russakovsky, O., J. Deng, H. Su, J. Krause, S. Satheesh, S. Ma, Z. Huang, A. Karpathy, A. Khosla,

571 M. Bernstein, A. C. Berg, and L. Fei-Fei, 2015, ImageNet Large Scale Visual Recognition Chal-

572 lenge: International Journal of Computer Vision (IJCV), **115**, 211–252.

573 Samuel, A. L., 1959, Some studies in machine learning using the game of checkers: IBM Journal

574 of research and development, **3**, 210–229.

575 Siler, D. L., and J. E. Faulds, 2013, Three-dimensional geothermal fairway mapping: Examples

576 from the western great basin, usa,: GRC Transactions, **7**, 327–332.

577 Szegedy, C., V. Vanhoucke, S. Ioffe, J. Shlens, and Z. Wojna, 2015, Rethinking the Inception Ar-

578 chitecture for Computer Vision.

579 Trainor-Guitton, W. J., A. Ramirez, X. Yang, K. Mansoor, Y. Sun, and S. Carroll, 2013, Value

580 of information methodology for assessing the ability of electrical resistivity to detect co2/brine

581 leakage into a shallow aquifer: International Journal of Greenhouse Gas Control, **18**, 101–113.

LIST OF FIGURES

582 1 PoroTomo survey geometry. Green dots represent source locations, red dots represent geo-

583 phone locations, and the blue line represents the surface DAS layout.

584 2 Consider a source that generates both P and S waves; this is a 2-D Homogeneous, flat-

585 layered, isotropic ray path example. The blue lines represent ray paths of the labeled waves, the

586 blue arrow represents the propagation direction of the wave, the green line represents a horizontal

587 reflector in the subsurface, and the yellow star represents the source. (a) Demonstration of P-P wave

588 effect on fiber using ray paths. Particle motion is inline with propagation direction (blue arrow).

589 The fiber will only record data at large offsets. (b) Demonstration of P-SV wave effect on fiber

590 using ray paths. Particle motion is perpendicular with the propagation direction (green arrows). The

591 fiber will only record data at short offsets.

592 3 Amplitude versus emerging angle for both geophone (blue) and horizontal DAS (red). An

593 emerging angle of 0° indicates a wave that is propagating perpendicular to the surface and an emerg-

594 ing angle of 90° degrees indicated a wave is propagating parallel to the surface. (a) Sensitivity with

595 respect to a P-wave at different emerging angles of horizontal DAS (red) and geophone z-component

596 (blue). (b) Sensitivity with respect to an SV-wave at different emerging angles of horizontal DAS

597 (red) and geophone x-component (blue).

598 4 Siler and Faulds (2013) fault density mapping within the PoroTomo Survey box. This

599 model was used as a reflectivity model for the experiments within this section.

600 5 Reflectivity model from Siler and Faulds (2013) extracted at the location of Well 56-A1

601 used for simulating data. Blue dots represent source locations and the red dots represent geophone

602 locations. DAS fiber was placed between the geophone locations.

603 6 (a) Resulting image from migrating geophone synthetic data. (b) Resulting image from

604 migrating DAS synthetic data. (c) Combined image from migrating DAS and geophone synthetic

605 data.

606 7 (a) Resulting image from migrating geophone synthetic data. (b) Resulting image from
607 migrating DAS synthetic data. (c) Combined image from migrating DAS and geophone synthetic
608 data.

609 8 (a) Examples of the automatically generated faults images used to train the CNN. (b) Ex-
610 amples of the automatically generated images that were not faults used to train the CNN.

611 9 Posterior reliability of information from CNN's calculated using Equation 3 using (a) a
612 vertical force and (b) a horizontal force. The objective is to maximize the percentages of true posi-
613 tives and negatives (green arrows) while minimizing the percentages of false positives and negatives
614 (red arrows). This is obtained by having better instruments as well as better classification.

615 10 Body wave (P-wave) velocity (m/s) model from sweep interferometry in 3-D perspective
616 (Matzel et al., 2017b).

617 11 Four layer model with a variety of structures used for data modeling. This model is used
618 as a density model for elastic modeling.

619 12 Results of migrating the reflectivity model (Figure 11) using the PoroTomo DAS acquisi-
620 tion shown on the right. The true reflectivity model is overlain and shown on the left. The slices on
621 each side are taken at the yellow cross shown on the map view of the acquisition.

622 13 Results of migrating the reflectivity model (Figure 11) using the PoroTomo geophone ac-
623 quisition shown on the right. The true reflectivity model is overlain and shown on the left. The
624 slices on each side are taken at the yellow cross shown on the map view of the acquisition.

625 14 Posterior reliability of information from energy norm filtering calculated using Equation 3
626 using a horizontal force. The objective is to maximize the percentages of true positives and nega-
627 tives (green arrows) while minimizing the percentages of false positives and negatives (red arrows).

628 15 New survey geometry proposed to test the effectiveness of surface DAS fiber. Green dots

629 represent source locations, red dots represent geophone locations, and the blue lines represent the
630 surface DAS acquisition.

631 16 Posterior reliability of information using a horizontal force and the Figure 15 acquisition
632 geometry.

633

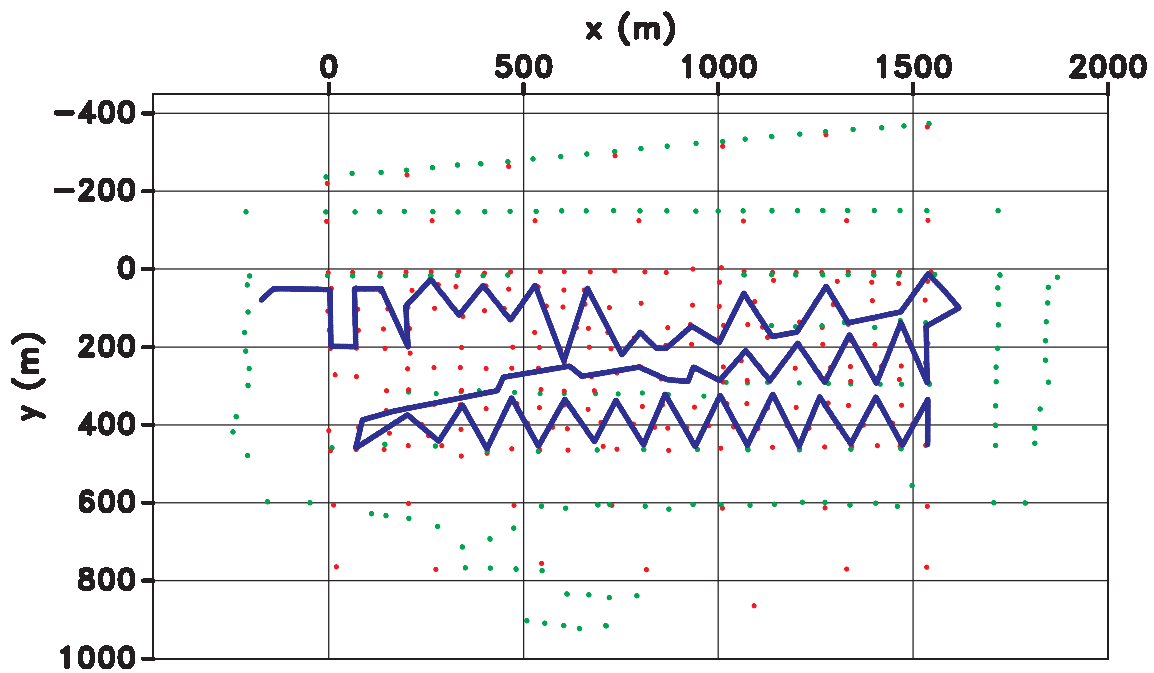
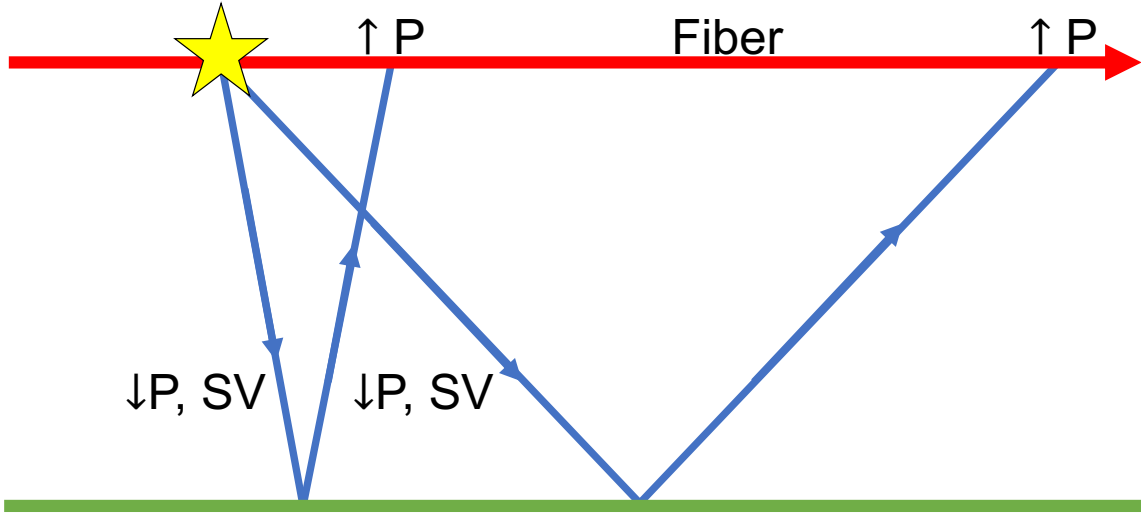
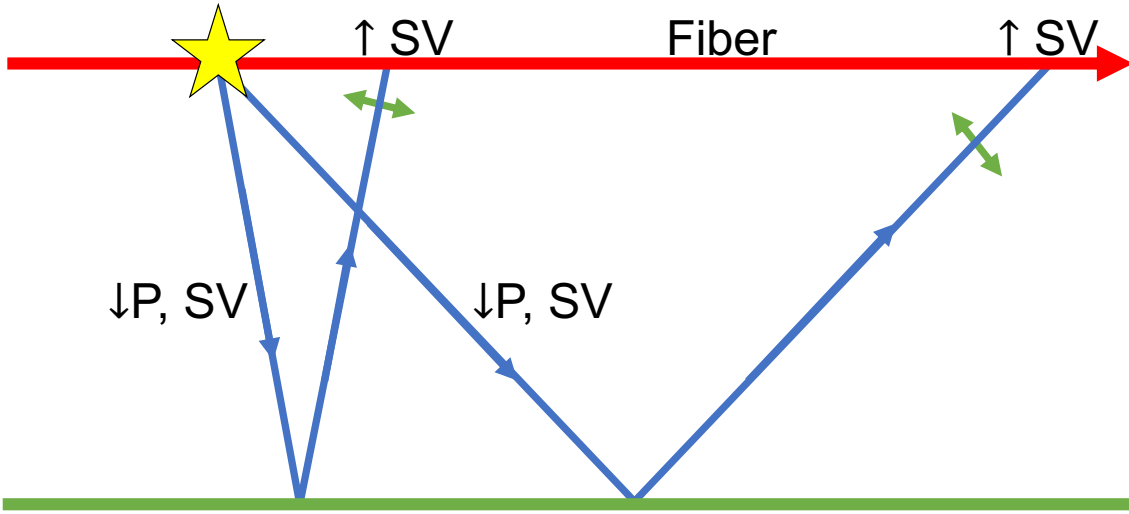


Figure 1: PoroTomo survey geometry. Green dots represent source locations, red dots represent geophone locations, and the blue line represents the surface DAS layout.

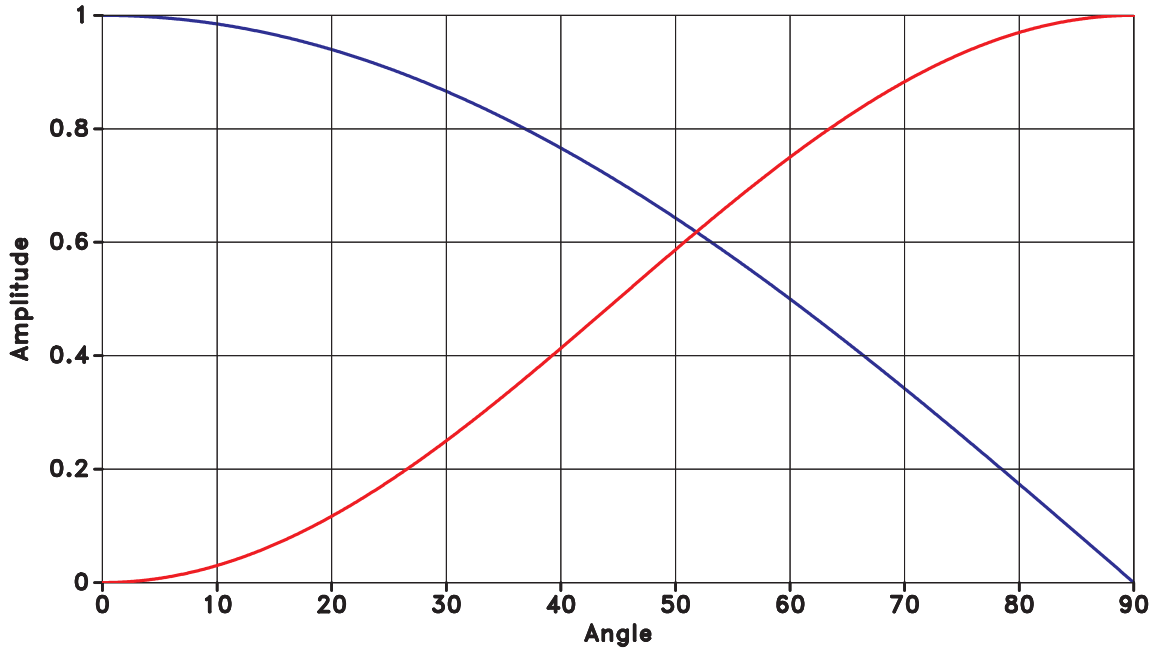


(a)

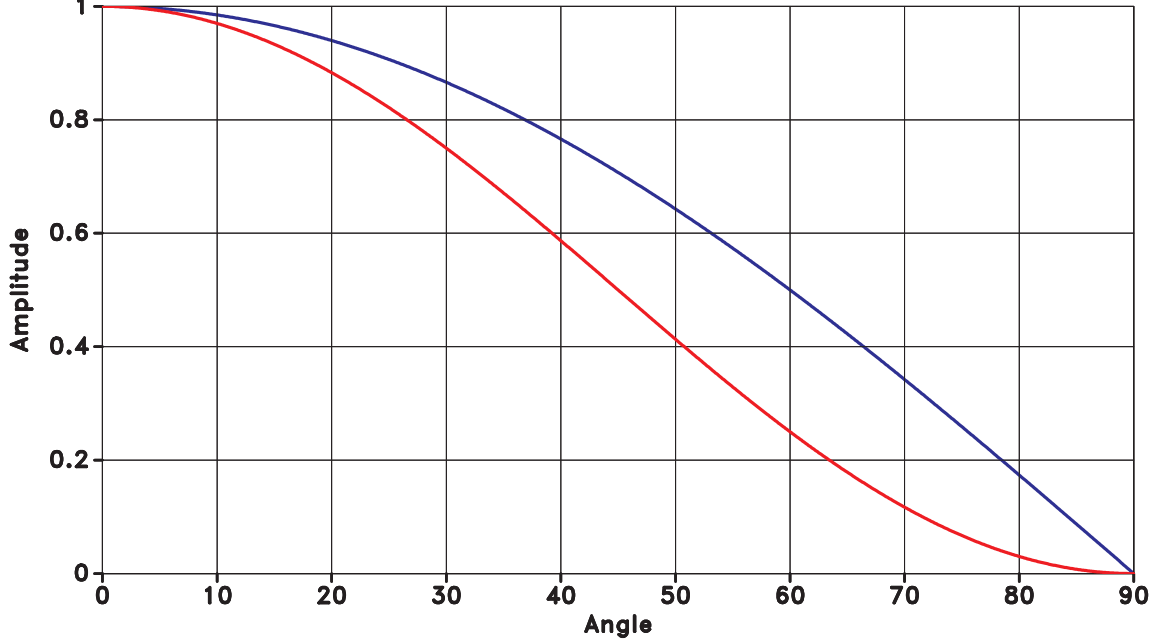


(b)

Figure 2: Consider a source that generates both P and S waves; this is a 2-D Homogeneous, flat-layered, isotropic ray path example. The blue lines represent ray paths of the labeled waves, the blue arrow represents the propagation direction of the wave, the green line represents a horizontal reflector in the subsurface, and the yellow star represents the source. (a) Demonstration of P-P wave effect on fiber using ray paths. Particle motion is inline with propagation direction (blue arrow). The fiber will only record data at large offsets. (b) Demonstration of P-SV wave effect on fiber using ray paths. Particle motion is perpendicular with the propagation direction (green arrows). The fiber will only record data at short offsets.



(a)



(b)

Figure 3: Amplitude versus emerging angle for both geophone (blue) and horizontal DAS (red). An emerging angle of 0° indicates a wave that is propagating perpendicular to the surface and an emerging angle of 90° degrees indicated a wave is propagating parallel to the surface. (a) Sensitivity with respect to a P-wave at different emerging angles of horizontal DAS (red) and geophone z-component (blue). (b) Sensitivity with respect to an SV-wave at different emerging angles of horizontal DAS (red) and geophone x-component (blue).

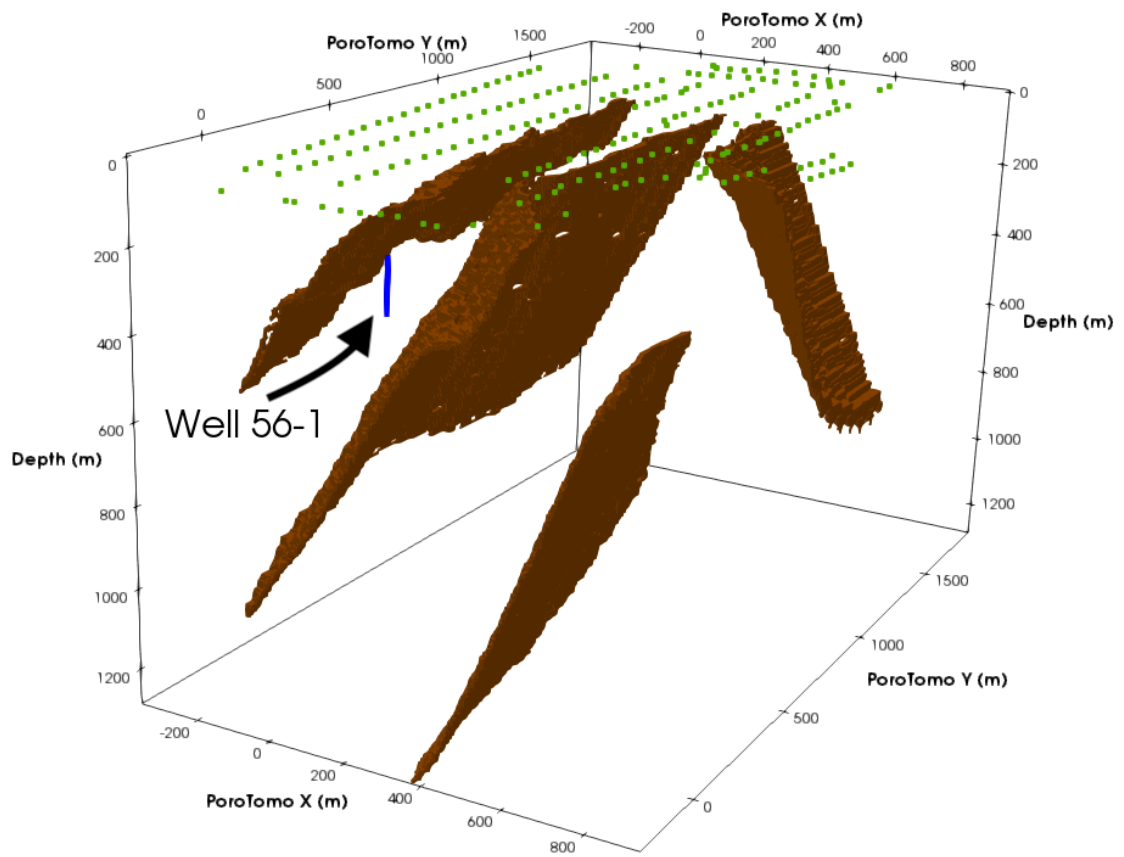


Figure 4: Siler and Faulds (2013) fault density mapping within the PoroTomo Survey box. This model was used as a reflectivity model for the experiments within this section.

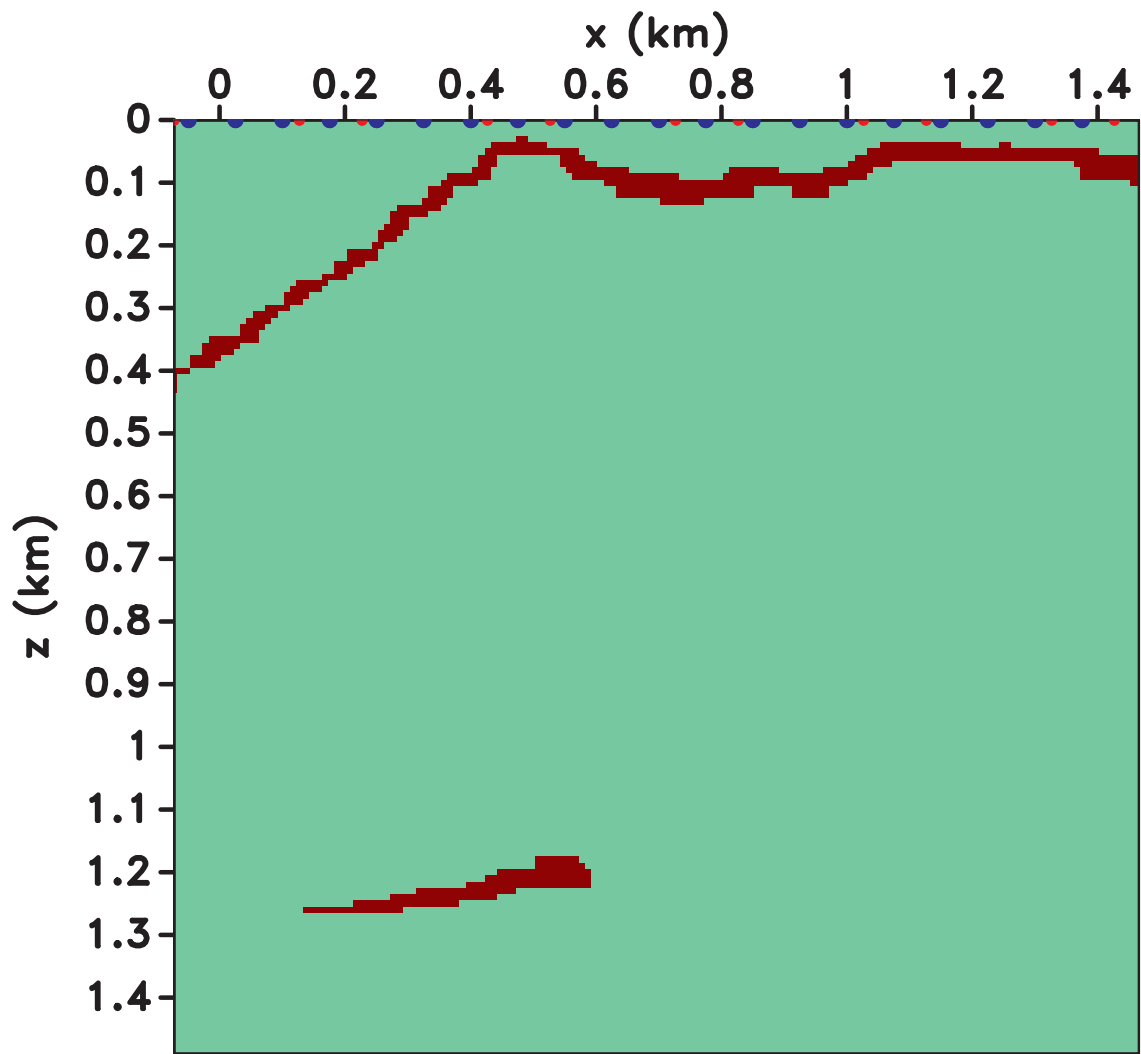


Figure 5: Reflectivity model from Siler and Faulds (2013) extracted at the location of Well 56-A1 used for simulating data. Blue dots represent source locations and the red dots represent geophone locations. DAS fiber was placed between the geophone locations.

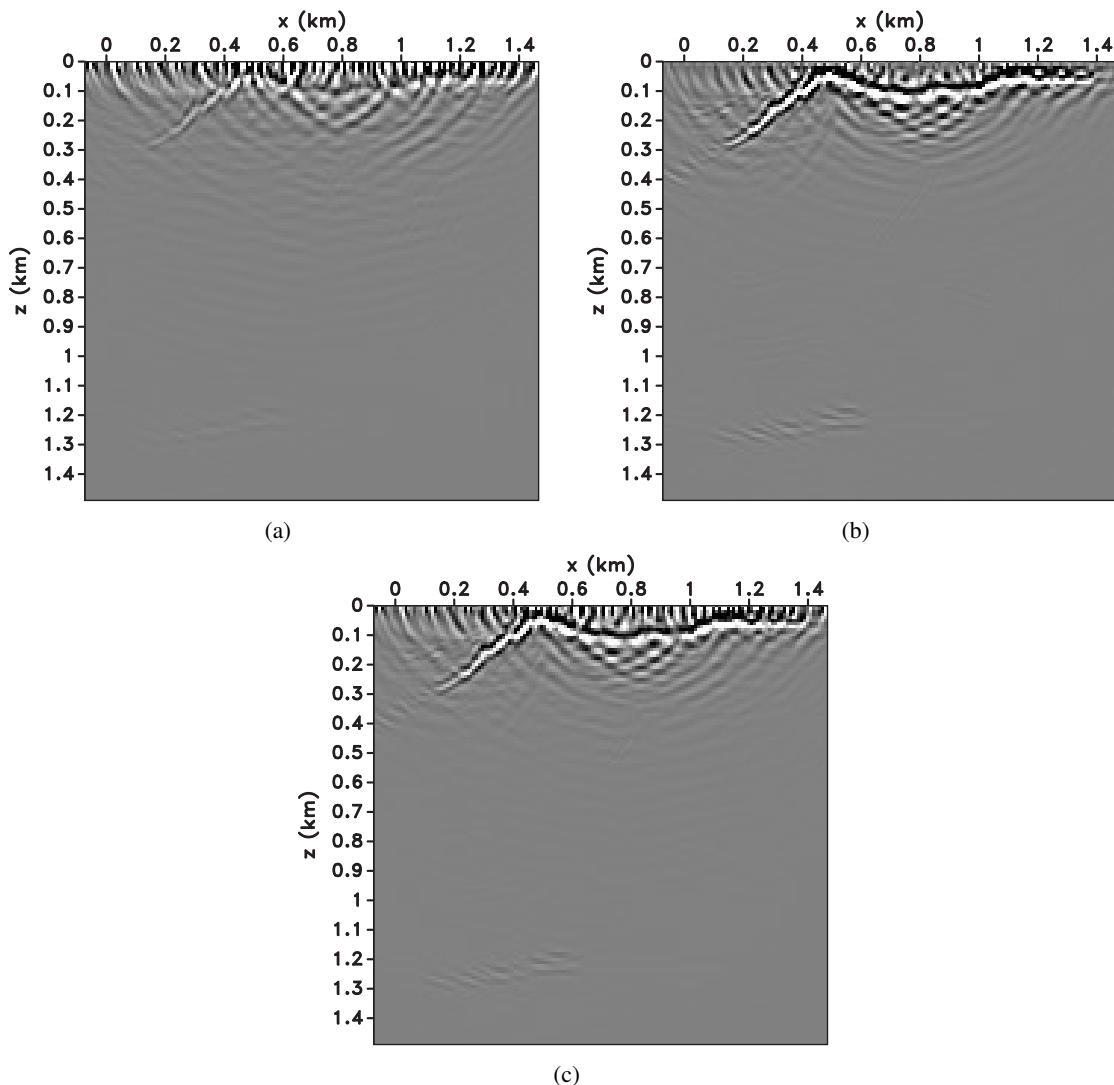


Figure 6: (a) Resulting image from migrating geophone synthetic data. (b) Resulting image from migrating DAS synthetic data. (c) Combined image from migrating DAS and geophone synthetic data.

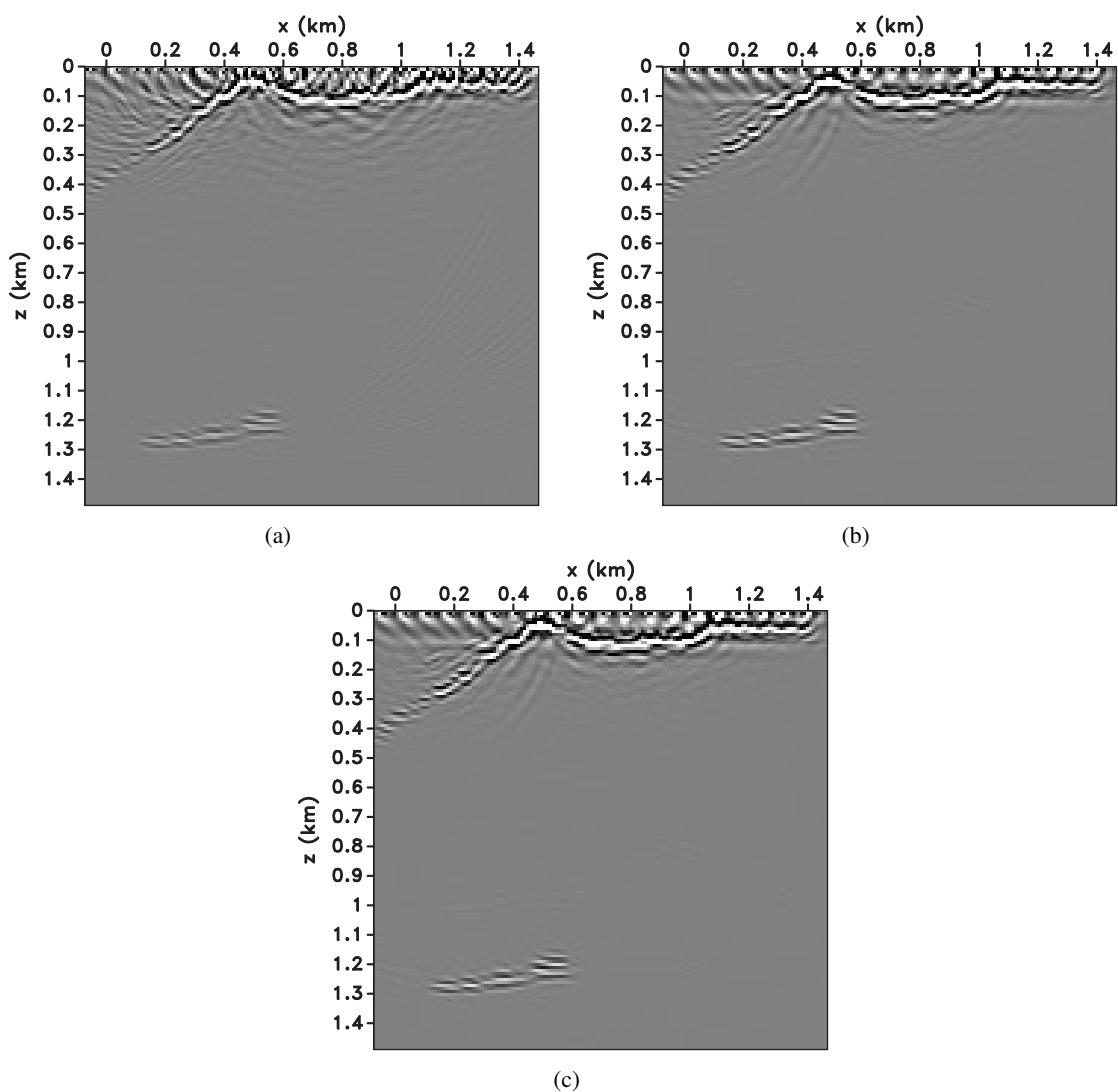
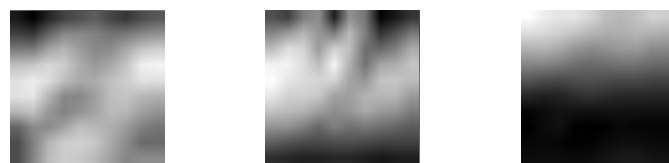


Figure 7: (a) Resulting image from migrating geophone synthetic data. (b) Resulting image from migrating DAS synthetic data. (c) Combined image from migrating DAS and geophone synthetic data.

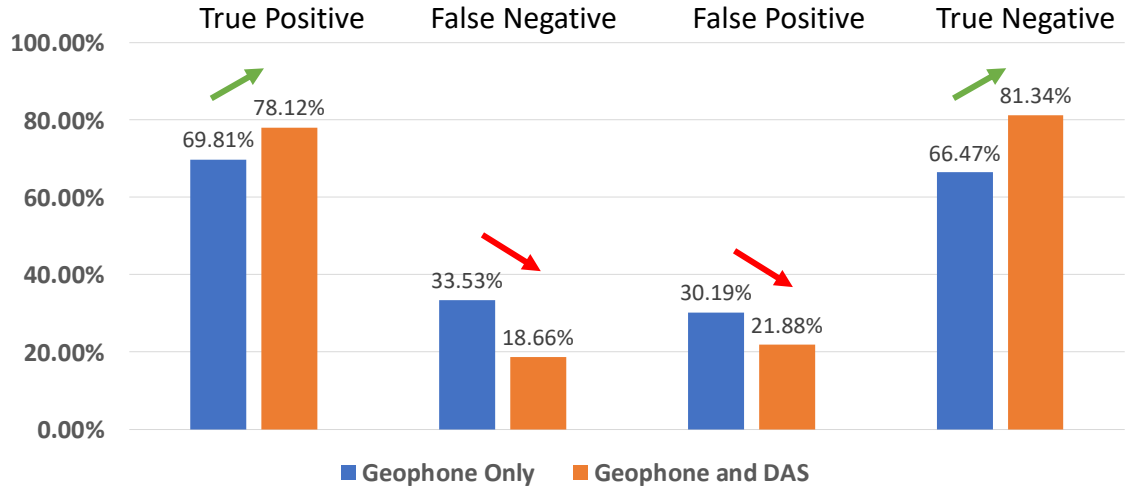


(a)

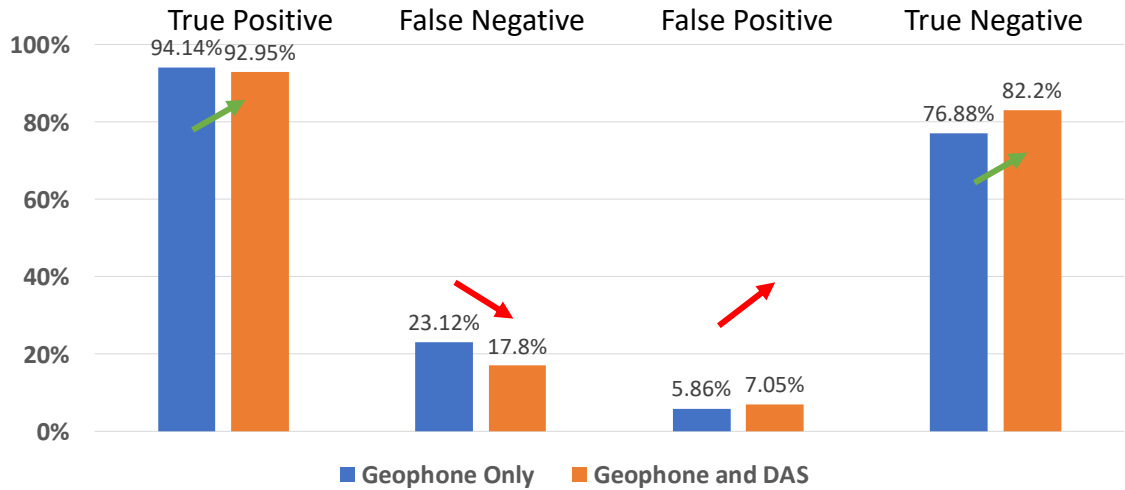


(b)

Figure 8: (a) Examples of the automatically generated faults images used to train the CNN. (b) Examples of the automatically generated images that were not faults used to train the CNN.



(a)



(b)

Figure 9: Posterior reliability of information from CNN's calculated using Equation 3 using (a) a vertical force and (b) a horizontal force. The objective is to maximize the percentages of true positives and negatives (green arrows) while minimizing the percentages of false positives and negatives (red arrows). This is obtained by having better instruments as well as better classification.

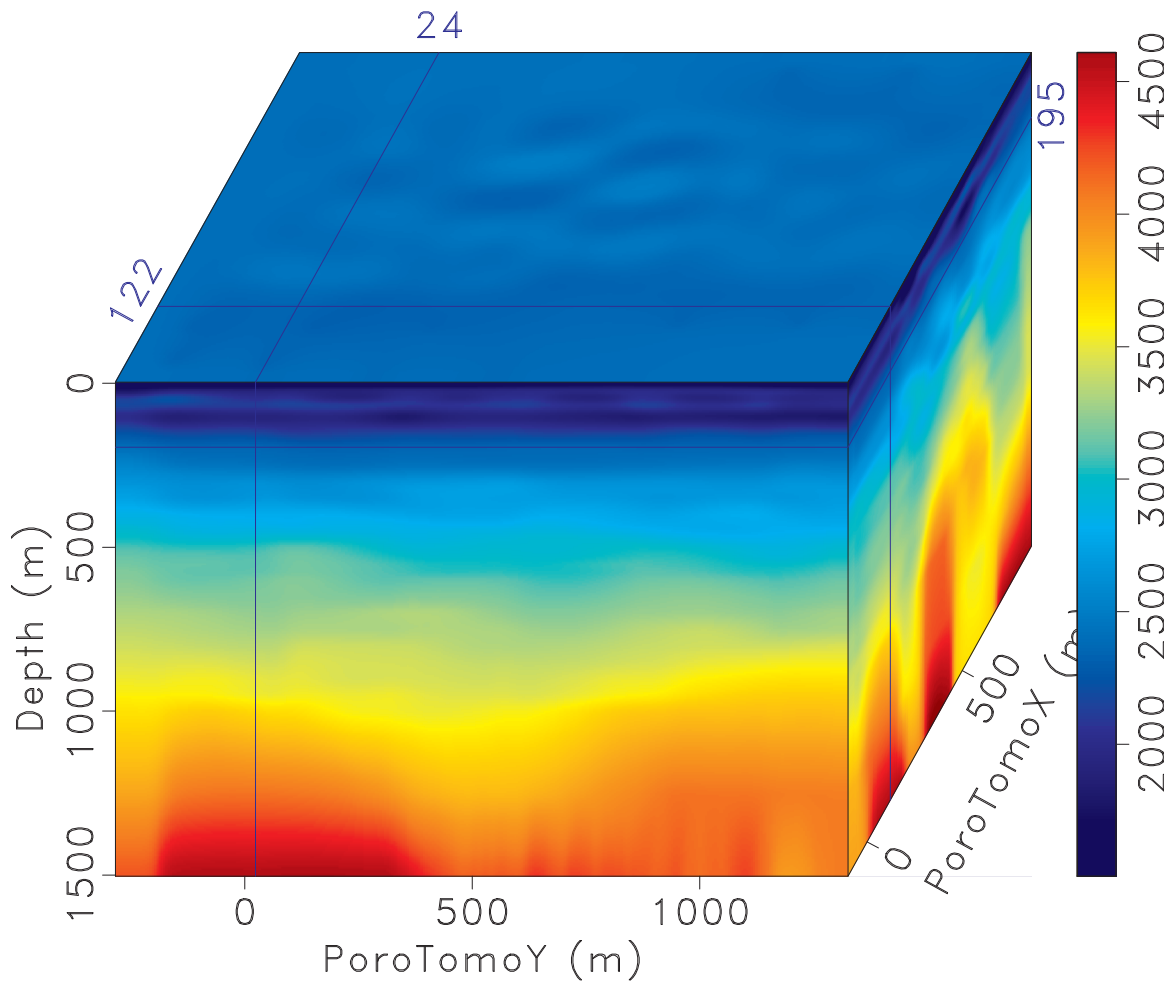


Figure 10: Body wave (P-wave) velocity (m/s) model from sweep interferometry in 3-D perspective (Matzel et al., 2017b).

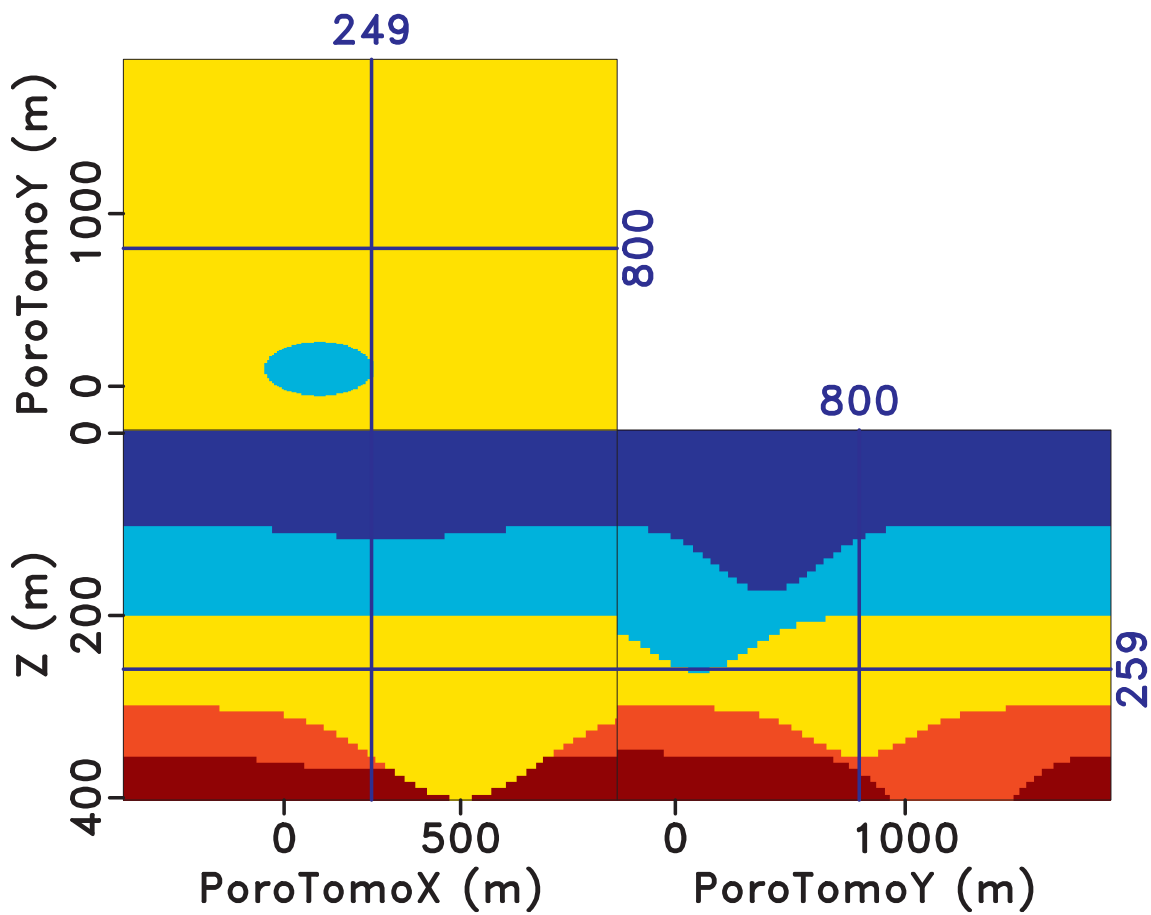


Figure 11: Four layer model with a variety of structures used for data modeling. This model is used as a density model for elastic modeling.

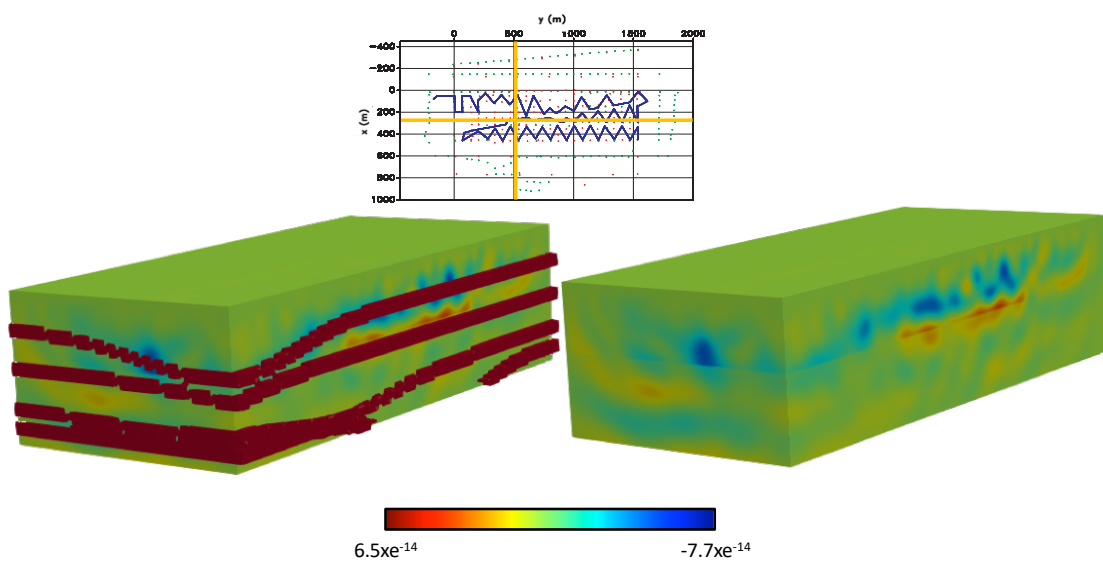


Figure 12: Results of migrating the reflectivity model (Figure 11) using the PoroTomo DAS acquisition shown on the right. The true reflectivity model is overlain and shown on the left. The slices on each side are taken at the yellow cross shown on the map view of the acquisition.

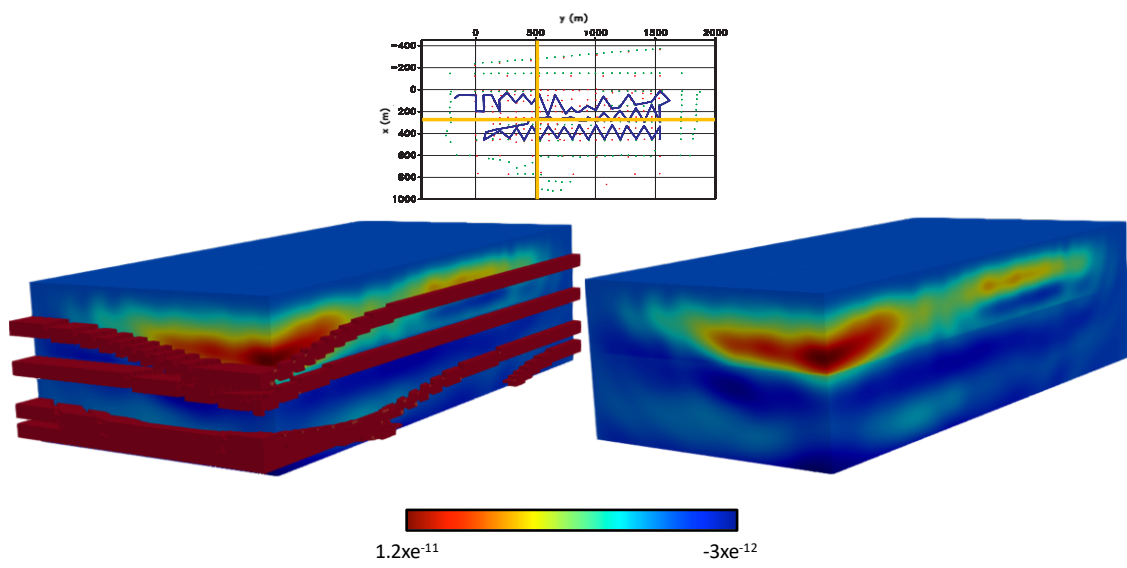


Figure 13: Results of migrating the reflectivity model (Figure 11) using the PoroTomo geophone acquisition shown on the right. The true reflectivity model is overlain and shown on the left. The slices on each side are taken at the yellow cross shown on the map view of the acquisition.

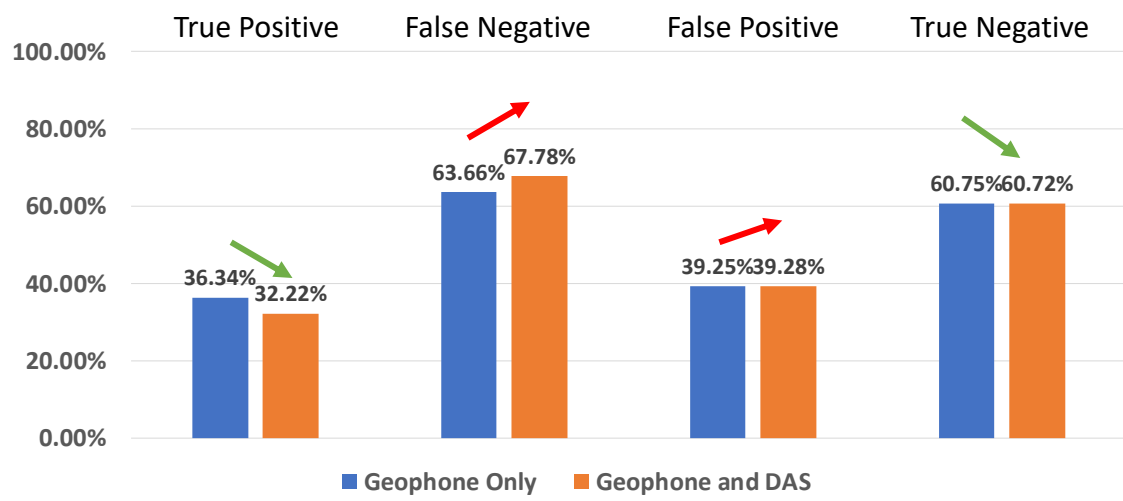


Figure 14: Posterior reliability of information from energy norm filtering calculated using Equation 3 using a horizontal force. The objective is to maximize the percentages of true positives and negatives (green arrows) while minimizing the percentages of false positives and negatives (red arrows).

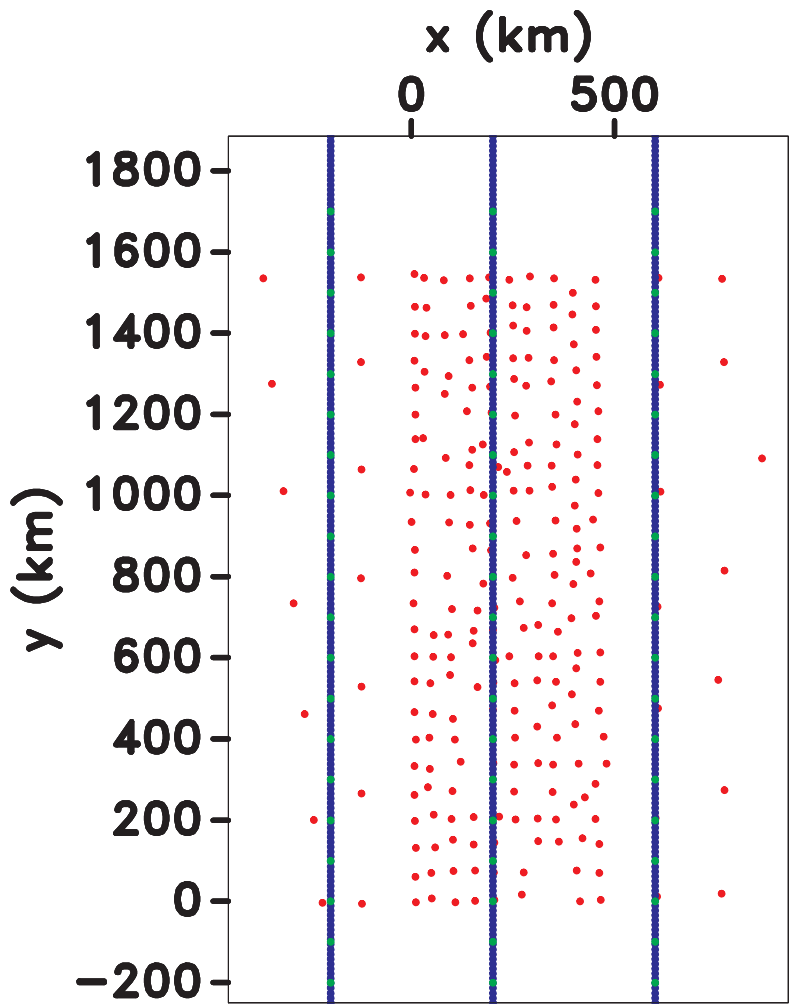


Figure 15: New survey geometry proposed to test the effectiveness of surface DAS fiber. Green dots represent source locations, red dots represent geophone locations, and the blue lines represent the surface DAS acquisition.

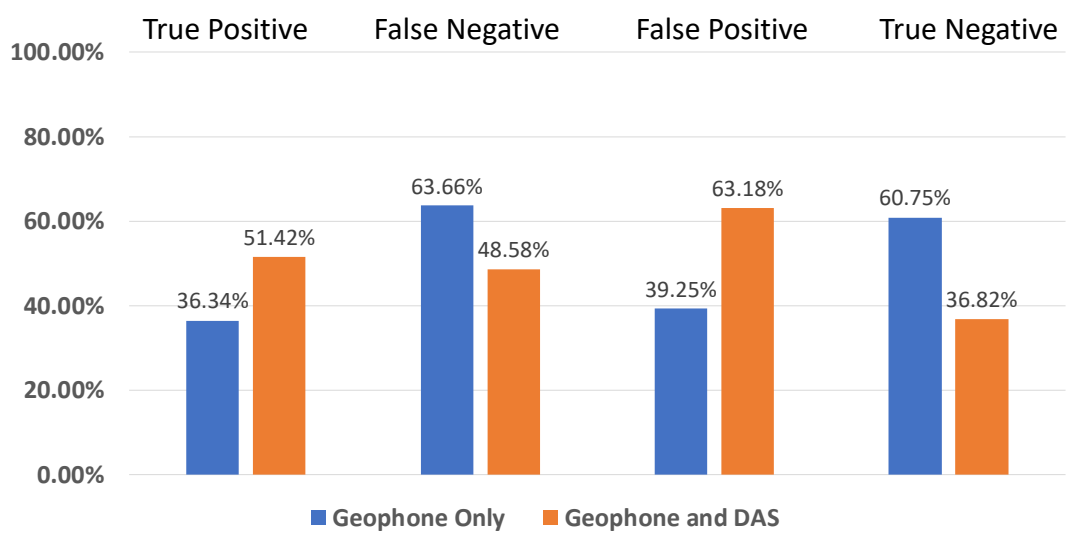


Figure 16: Posterior reliability of information using a horizontal force and the Figure 15 acquisition geometry.